Products and coke shape-selectivity during anisole disproportionation over HZSM-5

Nathan Pichot, Jean Wilfried Hounfodji, Michael Badawi, Valentin Valtchev, Svetlana Mintova, Jean-pierre Gilson, Anthony Dufour, Ludovic Pinard

Products and coke shape-selectivity during anisole disproportionation over HZSM-5

N. Pichot[1,2,4], J.W. Hounfodji[3], M. Badawi[3], V. Valtchev[4], S. Mintova[4], J-P Gilson[4], A. Dufour [2], L. Pinard[4]*

[1]Institut de Chimie des Milieux et Matériaux de Poitiers (UMR 7285, Université de Poitiers, France)

[2]Laboratoire Réactions et Génie des Procédés (UMR 7274, Université de Lorraine, France)

[3]Laboratoire de Physique et Chimie Théoriques (UMR 7019, Université de Lorraine, France)

[4]Laboratoire de Catalyse et Spectrochimie (UMR 6506, ENSICaen, France)

Abstract

Anisole conversion on an MFI zeolite (Si/Al = 43) at atmospheric pressure and 673 K is a model for the upgrading of bio-oils produced by catalytic fast pyrolysis (CFP) of biomass. Catalyst activity and selectivity are measured experimentally, while deactivation is studied experimentally and by DFT calculations.

Anisole dismutation is a Friedel-Crafts-type alkylation between two anisole molecules. Consecutive reactions produce phenol and methyl anisoles, cresols and xylenols, as primary, secondary, and tertiary products respectively. The resonance effect of the hydroxyl and methoxy groups, combined with the "product shape selectivity" of the zeolite, results in a high selectivity for p-methyl-anisole, o-cresol and 2,4 xylenol.

Coke deposition consists exclusively of methylphenols with 0 to 4 methyl groups. Their retention is due to steric hindrance for the larger ones and strong adsorption on stronger acid sites for the smaller ones, as confirmed by DFT calculations. Catalyst deactivation occurs by progressive fouling of the micropores rather than by poisoning.

Introduction

Petrochemicals are pervasive in our daily lives as plastics, packaging, clothing, digital devices, medical equipment, tires… and provide substantial benefits to society, including a growing number of applications in various cutting-edge, clean technologies critical to sustainable energy systems. They

are set to account for more than a third of the growth in oil demand by 2030 and nearly half by 2050. At the same time, transportation fuels demand should decrease, due to the combined effects of better fuel economy, increasing use of public transport, alternative fuels, and electrification. Hence, the landscape for petrochemical, oil, and gas industries is evolving to develop more "high-value chemicals" (HVCs), such as aromatics. [1–5]

The majority of BTX (Benzene, Toluene, Xylene, etc.) is currently provided by catalytic reforming of desulfurized naphtha and non-catalytic steam cracking of various oil cuts. The catalytic fast pyrolysis (CFP) of biomass represents an interesting route to green aromatics and olefins by mimicking the fluid catalytic cracking of crude oil. [6–8] The pyrolysis is conducted in a dual fluidized bed on a zeolite catalyst; the latter shifts the chemical composition of bio-oils to petroleum-compatible products. The volatile oxygenates formed by biomass pyrolysis diffuse within the catalyst particles and contact the catalytic acid sites to form the targeted products (aromatics, olefins) but also coke and gas (mainly CO, CO_2)[9]. Despite the growing interest in biomass CFP, this process is still in its infancy compared with other thermochemical technologies (gasification or combustion). Some technologies are close to commercialization (Anellotech/Axens, BioBTX, RTI International [10], …), but require the development of more stable catalysts with increased BTX selectivity. [11,12]

Indeed, the most important economic and technical problem of this emerging process remains the deactivation of the zeolite catalyst. [13-16] This deactivation mostly occurs by coke deposition, i.e. polyaromatic hydrocarbons (PAH). Jia et al. studied the molecular composition of coke deposited after oak CFP. [6] After mineralization of the zeolitic framework with hydrofluoric acid, and recovery of the molecules released by a liquid-liquid extraction with dichloromethane, two fractions are obtained: soluble and insoluble. They showed that the soluble portion consisted mainly of mono and bicyclic aromatics (alkylbenzenes and alkylnaphtalenes). In contrast, the insoluble portion contained mostly polyaromatics, some oxygenated compounds and molar masses up to 1000 $g.mol^{-1}$. Coke is either found in the micropores and mesopores (internal coke) or in a less confined environment (external coke). The latter two have a less detrimental effect than the first one. [6] Therefore, mastering catalyst stability is essential to control selectivity and activity. Therefore, there is a strong incentive to understand the mechanisms leading to any loss in activity and/or selectivity, as well as find preventive measures and regenerative solutions to develop cheaper and cleaner processes. [13–15] The catalyst regeneration has been partially studied by Prasomsri et *al.*, who found a recovery of activity for an HY zeolite flushed with tetralin: the H-donor solvent, when flushed alone, would help to regenerate some of the active site; when anisole is co-fed tetralin, the initial conversion is fully recovered. [16]

Biomass CFP is modelled like the well-established FCC (Fluidized Catalytic Cracking) process, to upgrade otherwise unusable heavy oil fractions. [17–19] CFP aims to produce a similar slate, by breaking down lignocellulosic compounds. Some differences exist between the two processes, the first and main being that CFP feedstock contains lots of oxygen, which affects, of course, the reactions involved in the upgrading, but also could affect the deactivation of the catalyst, notably the nature of coke deposition in the channels. Graça et *al.* showed that co-feeding phenol to FCC feedstock further hindered the activity of MFI zeolite, by phenol adsorption on active sites; other effects occur, such as an increase in coke amount, as well as composition (aromaticity, size). [13,20]

Among all the studied catalysts, H-ZSM-5 zeolite has shown interesting selectivity in deoxygenated aromatics due to its moderate pore openings, internal pore space and steric hindrance [11,12,21–24] but a lot of coke is produced. It can poison the active sites ("poisoning") or block their access. Pore blocking is more harmful than poisoning, since one coke molecule can block access to several acid sites. Tri-dimensional zeolites (such as the H-ZSM-5 type MFI) are more resistant to coking than mono-dimensional zeolite (e.g., MOR or ERI), because more options to enter and exit the porosity are offered to reactants and products, respectively. [25]

Lignocellulosic biomass, when pyrolyzed, releases abundant oxygenates in methoxy functional groups (guaiacol, syringol, and derivatives). [9,22] Since the methoxy group is its only functional group, anisole (or methoxybenzene) is a logical model compound to investigate the reactivity of methoxy-substituted compounds present in the gas phase during the fast pyrolysis of lignin. [26,27]

The present work aims to answer the following questions:

1) How do hydroxyl and methoxy groups affect the catalyst's activity, selectivity, and deactivation?
2) How does catalyst deactivation proceed during anisole conversion (pore blocking, active site poisoning, ...)?

An experimental approach coupled with DFT calculations is used to probe the three features of a catalyst, namely activity, selectivity, and stability. In particular, the effect of time on stream (reaction time, ToS, h) and contact time (W/F, $g_{cata}.h.g_{feed}^{-1}$) on catalyst activity and product selectivity are assessed as well as deactivation by coke deposition. For the latter, coke composition, its kinetics of formation and affinity for the active sites will receive a particular attention.

Experimental

***Catalyst and reagent**:* The ZSM-5 (Si/Al = 43) zeolite is provided by Zeolyst, originally in NH_4^+ form. Calcination is performed to obtain the protonic form under N_2 (P_{atm}, 100 mL.min^{-1}) at 373 K for an hour (5 K.min^{-1} from ambient) for water removal, then under air (P_{atm}, 100 mL.min^{-1}) at 823 K for 6 hours (10 K.min^{-1}). The micropore volume measured by N_2-physisorption at 77 K and the concentration of Brønsted acid sites probed by pyridine thermodesorption at 423 K are 0.164 cm^3.g^{-1} and 281 µmol.g^{-1}, respectively. Anisole (>99%) from Sigma Aldrich is used as reagent.

Catalytic tests: Anisole transformation on H-ZSM-5 is carried out in a continuous down-flow tubular glass fixed bed reactor. It is 75 cm long, with an internal diameter of 0.45 cm. Before each test, the catalyst is compacted (under a press, 500 kg), then crushed and sieved to obtain homogeneous particles of 0.2 <ø< 0.4 mm diameter. The mass of catalyst in the fixed bed was varied between 25 and 100 mg. At first, the reactor is heated at 373 K (1 K.min^{-1} from ambient), with a 1 h plateau, to avoid any steaming damage from adsorbed water. After this water desorption step, heating is resumed at 1 K.min^{-1} until 673 K, with a stabilization time of 1 h. Anisole is then continuously injected in liquid form (0.01 mL.min^{-1} with a Metrohm 725 Dosimat and instantaneously vaporized upon entry in the reactor. The length and design of the reactor allow for higher residence time, and better reactant heating. The operating conditions are as follows: $P_{anisole}$ = 0.048 atm, N_2 influx = 100 mL.min^{-1}, T = 673 K. All lines after the reactor are heated at 623 K to avoid condensation of reactant and products.

Reaction products are sampled in a 10 port (500 µL each) valve (at 0.5 min, then 2.5, 4.5, 9.5, 14.5, 24.5, 34.5, 44.5, 54.5, 64.5 min), then injected in a GC-FID from Scion (456-GC, Scion5-MS column, 30 m- 0.25 mm- 25 µm). These reaction products are identified by GC-MS (GC-QTOF (Agilent)). All the quantitative analysis was done on the basis of the FID detector. Conversion and molar yields are calculated from equation 1 &2 .

$$X\ (\text{mol}\%) = \left(1 - \frac{\frac{A_{Anisole}}{7}}{\frac{A_{tot}}{\bar{n}_{Ctot}}}\right) * 100 \qquad \textbf{(eq 1)}$$

where $A_{Anisole}$ is the area of the anisole peak (GC-FID); 7 the number of carbon atoms in anisole; A_{tot} the sum of all peak area in the chromatogram; $\bar{n}_C$ the mean number of carbon atoms per molecule in the product fraction.

$$Y_i\ (\text{mol}\%) = \left(\frac{\frac{A_i}{n_{Ci}}}{\sum_i\left(\frac{A_i}{n_{Ci}}\right)}\right) * 100 \qquad \textbf{(eq 2)}$$

where A_i is the area of the target product's peak; n_{Ci} the number of carbon atoms in the target product.

For all experiments, the molar yield into methane and light alkanes (cracking products) is negligible (< 0.5 %). The carbon balance is higher than 95%.

Once the anisole injection is finished, the catalyst undergoes stripping under N_2 for 15 minutes at 673 K. The reactor is removed immediately from the oven and quenched under air flow.

Spent catalyst characterization: Nitrogen sorption measurements are carried out at 77 K on the zeolite after the catalytic tests with a Micromeritics 3Flex apparatus. The spent samples are degassed at room temperature under vacuum for 15 h before the sorption measurements. The micropore volume (V_{micro}) is calculated from the t-plot curve using the Harkins-Jura method and a thickness range between 4.5 and 5.8 Å.

Pyridine adsorption followed by infrared (IR) spectroscopy (Nicolet Magna FTIR iS50 spectrometer) is used to investigate the acid site properties at 423 K. [28,29] The spent catalysts are first pressed into thin wafers and activated in situ in the IR cell under secondary vacuum (10^{-6} mbar) at 423 K. The interaction between the pyridine molecules and the acid sites of zeolites is responsible for the appearance of some characteristic bands of pyridine adsorbed on Brønsted and Lewis acid sites in the 1300-1700 cm^{-1} region, corresponding to pyridinium ions (1490, 1545, 1640 cm^{-1}) and pyridine coordinated to Lewis acid sites (1455, 1490, 1600-1630 cm^{-1}). The concentration of different acid sites is calculated from the following formula, extracted from the Beer-Lambert-Bouguer law: $= \frac{A}{\varepsilon} \times \frac{S}{m} \times 1000$, with C the acid sites concentration (µmol.g^{-1}), A the band area (absorption.cm^{-1}), S the wafer surface (2 cm^2), m the mass of the wafer (mg), and ε the molar extinction coefficient (cm.µmol^{-1}). Molar extinction coefficients are previously determined to be respectively 1.13 cm.µmol^{-1} and 1.28 cm.µmol^{-1} for Brønsted and Lewis acidities. [29]

Coke content is assessed first by TDA-TGA (SDT Q600): around 20 mg of the coked sample is placed into a platinum crucible, onto one of the scales; under air with an isotherm at ambient temperature for 5 minutes, then 10 K.min^{-1} until 1173 K.

Carbon, hydrogen, and oxygen contents in coke are assessed using elemental analysis by atomic absorption spectroscopy (Flash EA 1112/Flash 2000 Thermo).

Coke trapped within the micropores is extracted, consisting in the destruction and dissolution of the zeolitic structure by HF (40 wt.% in water) at room temperature. [30] Then, boric acid is used to

neutralize F^- ions, and sodium bicarbonate is added to neutralise the mixture. Finally, Dichloromethane (CH_2Cl_2) is poured in, under stirring, to facilitate the liquid-liquid extraction of the carbonated molecules from the aqueous to the organic phase.

After extraction, the molecular (qualitative) composition of soluble coke is assessed using GC-MS (GC-QTOF, Agilent), while the quantification is carried out using GC-FID (Agilent Technologies 7820A, and Agilent technologies HP-5 column).

Atomistic simulations: DFT calculations are performed using the Vienna Ab initio Simulation Package (VASP) [31]. The semi-local exchange-correlation functional of Perdew-Burke-Ernzrhof (PBE) in the general gradient approximation (GGA) is used. [32] The electron-ion interactions are described using the Projected Augmented Wave (PAW) method, with a cut-off energy set to 450 eV. [33] Kohn-Sham equations are solved self-consistently with a convergence criterion of 10^{-6} eV. The ionic relaxation is systematically conducted until the forces applied on each atom are smaller than 0.02 $eV.A^{-1}$. Considering the large cell size, the Brillouin zone integration large is performed using the Γ-point only. Furthermore, to predict accurately the adsorption energies of the different molecules considered, dispersion interactions are accounted using the D2 correction. [34,35]

The adsorption energies of the different molecules in the zeolite, ΔE_{ads}, are computed using the total energies of the bare zeolite $E_{zeolite}$, of the single molecule in the gas phase E_X, and of the molecule adsorbed in the zeolite $E_{zeolite\text{-}X}$, as follows (**eq. 3**):

$$\Delta E_{ads} = E_{(zeolite-X)} - E_{(zeolite)} - E_{(X)} \qquad \textbf{(eq. 3)}$$

In order to understand the mechanisms that govern adsorption, knowledge of the interactions involved in the adsorption process is very important. They are classified into two categories: van der Waals (more precisely London, or so-called dispersion related to the polarizability of the molecules) forces and electrostatic forces.

The contribution of London dispersion interactions, ΔE_{disp}, to the total interaction energy, is calculated as follows (**eq. 4**):

$$\Delta E_{disp} = E_{disp\,(zeolite-X)} - E_{disp\,(zeolite)} - E_{disp\,(X)} \qquad \textbf{(eq. 4)}$$

where the energies considered are, for each term, the contribution of dispersive interaction to the total energy.

Results and Discussion

Activity and selectivity of H-ZSM-5 (43) catalyst: The transformation of anisole (methoxybenzene) takes place at 673 K on the H-ZSM-5(43) catalyst. **Figure 1a** shows the evolution of anisole conversion as a function of time-on-stream (ToS), at three contact times ranging from 0.04 to 0.17 $g_{cata}.h.g_{feed}^{-1}$. As expected, the longer the contact time, the higher the deactivation rate. **Figure 1b** displays the test of the first-order rate equation (i.e. $|-\ln(1-X_t)|$ vs W/F) at different ToS. Straight lines through the origin are obtained regardless of ToS, indicating that the bimolecular transformation of anisole follows an apparent first order reaction. The time evolution of the kinetic rate ($k_{anisole}$) is shown in **Figure 1c**. $k_{anisole}$ ($g_{feed}.h^{-1}.g_{cata}^{-1}$) evolves according to an exponential decay function with a horizontal asymptote emerging after only a few minutes of operation. (**eq. 5**)

$$k_{anisole} = 11.2\, e^{-11.1t} + 3.23 \qquad \textbf{(eq.5)}$$

Two distinct regimes occur: a fast deactivation followed by a steady state, suggesting that the catalyst no longer undergoes any change, at least with respect to the rate of anisole conversion. Notably, the deactivation remains relatively low compared to the FCC catalyst (order of magnitude of a few seconds [36,37]).

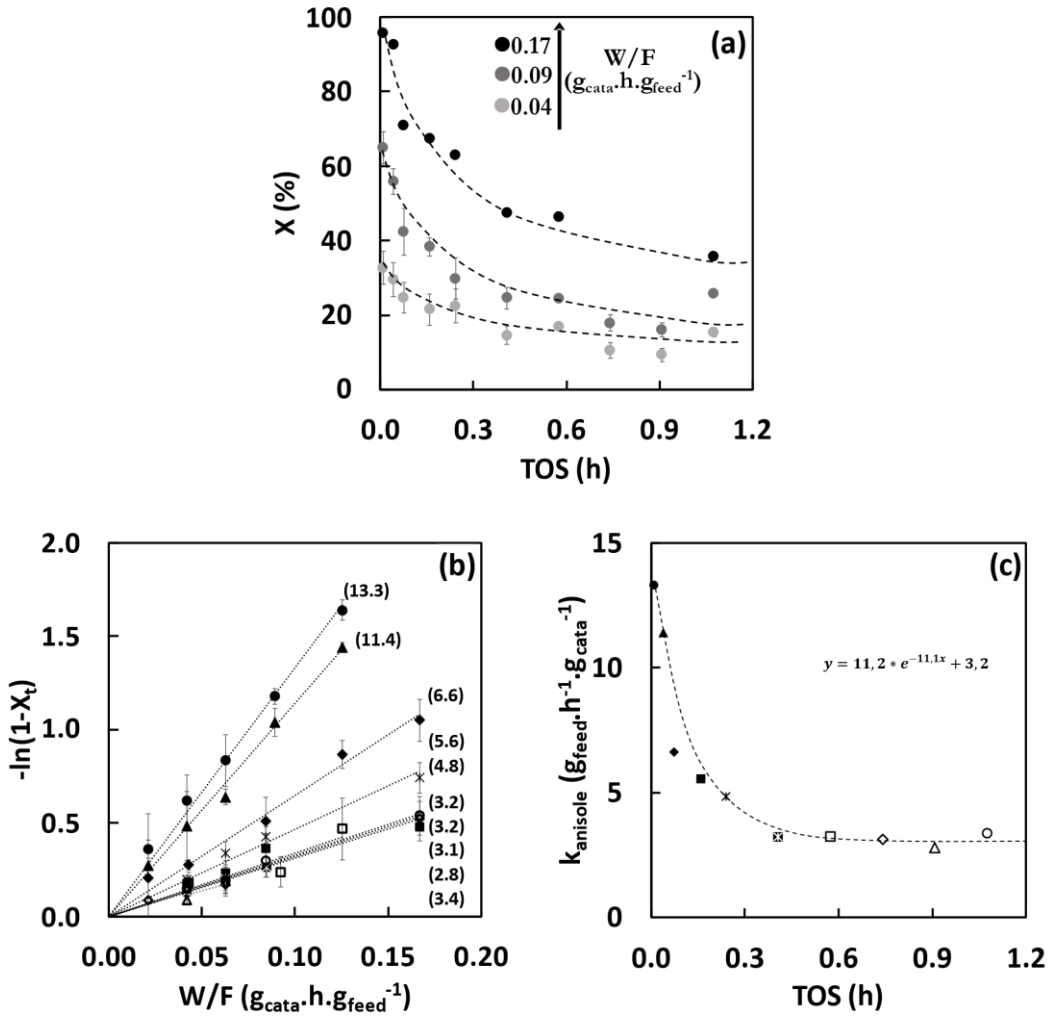

Figure 1: **(a)**: Anisole conversion as a function of time-on-stream obtained at different W/F and at 673 K **(b)**: Test for the first-order rate equation at various ToS (h) **(c)**: Time evolution of $k_{anisole}$. *Each data point corresponds to 2 to 3 experiments.*

Anisole transformation leads to phenol (**Ph**), methylanisoles (**MA**), cresols (**Cr**), xylenols (**Xol**), and aromatics (**Ar**), such as benzene, toluene, xylene. **Figure 2** shows the evolution of the formation of these products for different ToS and various contact times. The quasi-absence of methane in the products means that the cleavage of alkyl aryl ethers does not occur, as mentioned by Guisnet and coll. [38,39]

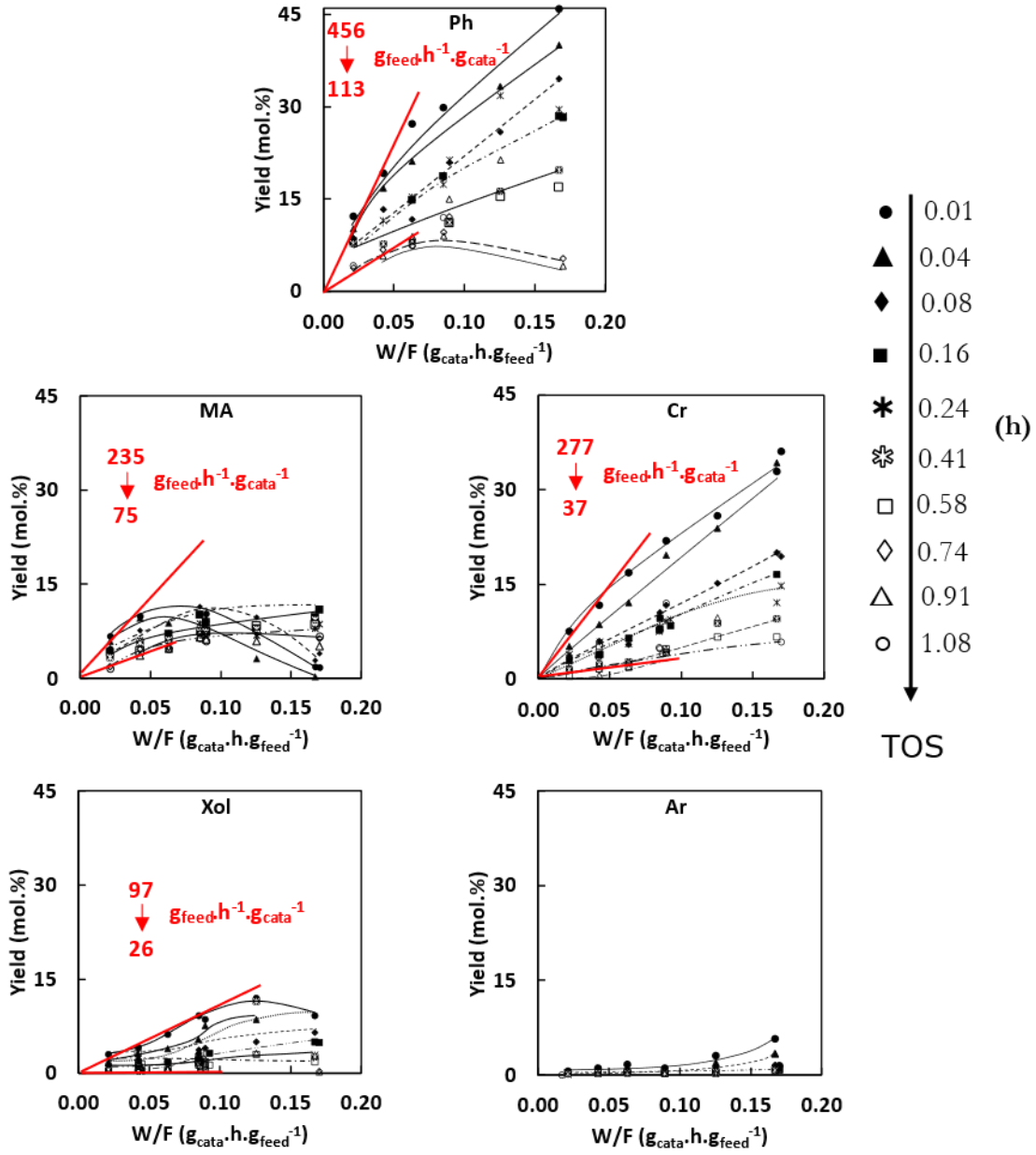

Figure 2: Molar yields for phenol (Ph), methylanisoles (MA), cresols (Cr), xylenols (Xol) and aromatics (Ar) as a function of contact time and at different time-on-stream. *(Lines are only drawn to guide the eye).*

On the fresh catalyst, phenol and cresol are the main products and their molar yields are proportional to contact time. Upon catalyst deactivation, the cresols yield decreases but remains proportional to W/F, whereas phenol yields go through a maximum. On the fresh catalyst and at low contact time, the yield of methylanisoles is also proportional to contact time and is in the same proportions as those of phenol and cresols. Indeed, the initial formation rates of phenol (456 $g_{feed}.h^{-1}.g_{cata}^{-1}$) is almost twice as high as those of methylanisoles (MA) and cresols (Cr), which are in the same

range ca 250 $g_{feed}.h^{-1}.\ g_{cata}^{-1}$, respectively. The successive transformations of methylanisole appear only at high contact time on the fresh or slightly deactivated catalyst. As for the other oxygenated products, the yield of xylenols is also proportional to contact time, but with a kinetic rate cut by half (97 $g_{feed}.h^{-1}.\ g_{cata}^{-1}$). Deactivation is detrimental to this formation. The yield of aromatics is low even at high contact time, and almost zero on the deactivated catalyst. All these evolutions agree with earlier observation by Zhu et al. [40]

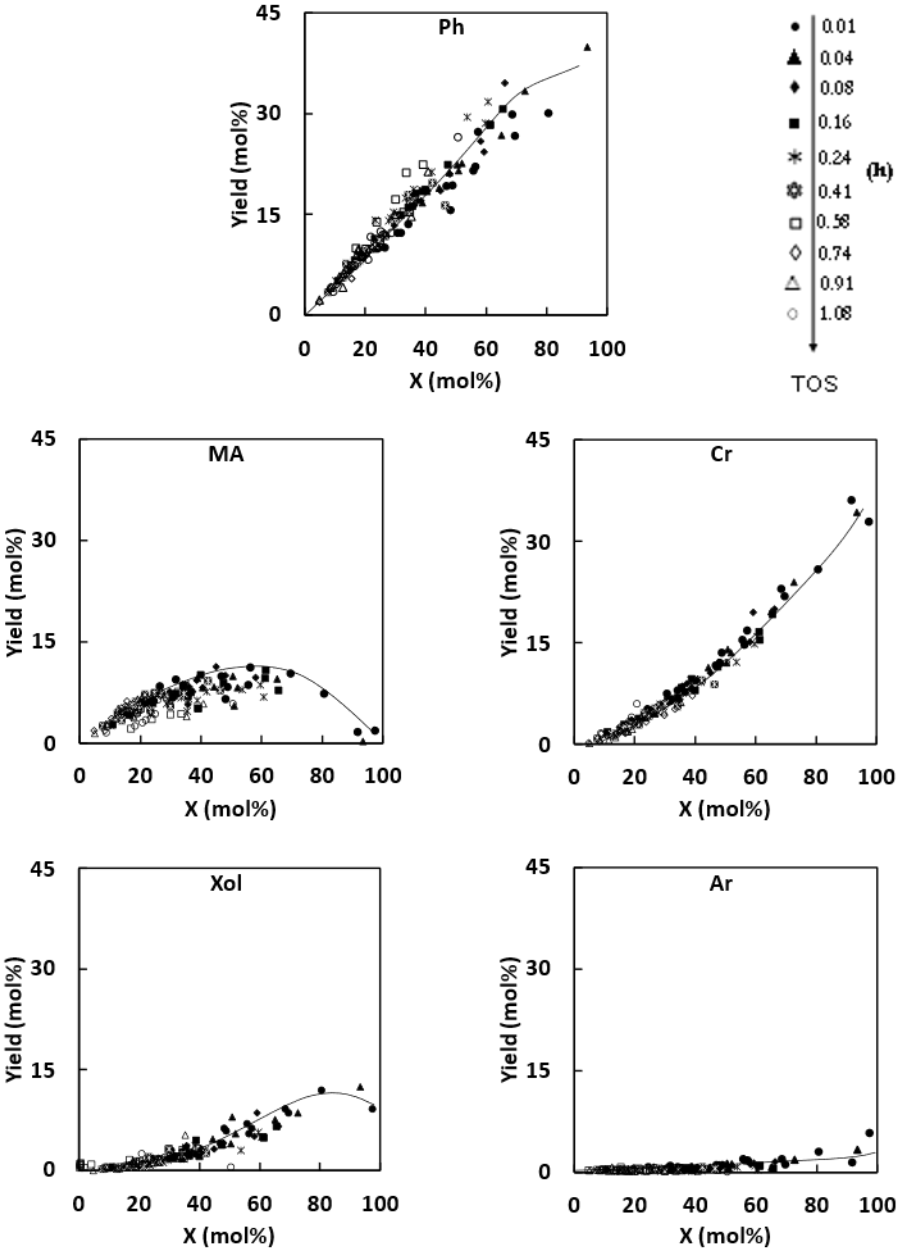

Figure 3: Molar yields into phenol (Ph), methylanisoles (MA), cresols (Cr), xylenols (Xol) and aromatics (Ar) as a function of anisole conversion (%). (*Lines are only drawn to guide the eye*).

These variations in selectivity could result from a conversion effect, rather than from deactivation with ToS. **Figure 3** illustrates this assertion by plotting product molar yields as a function of anisole conversion over both fresh and deactivated catalysts.

Product yields depend more on anisole conversion than on the degree of catalyst deactivation. Phenol and methylanisoles are the primary products of the reaction. Cresols are secondary product that is formed just after a low conversion of anisole (< 5 %) and xylenols are tertiary products that appears when the conversion is higher (> 20 %). As for aromatics, they are minor products formed at high conversion (> 40%).

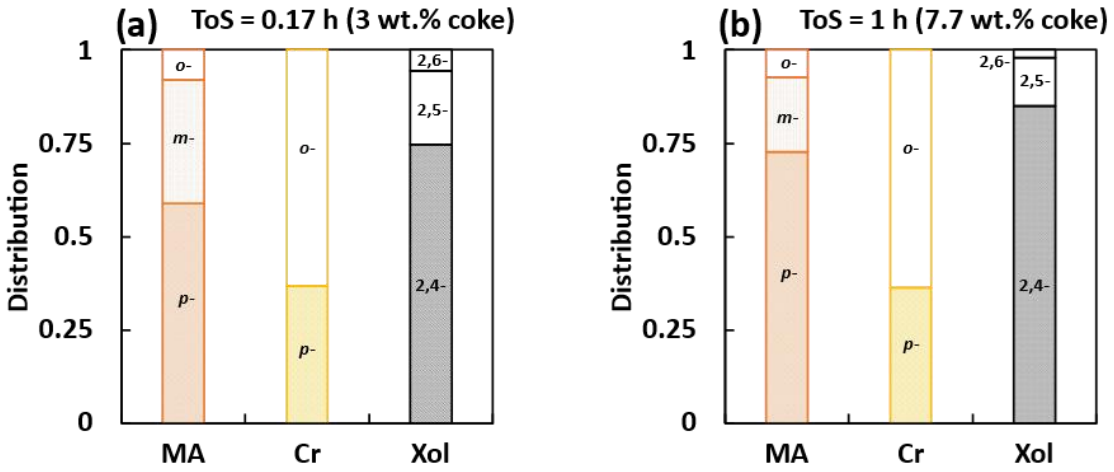

Figure 4: Distribution of the desorbed isomers of methylanisoles (MA), cresols (Cr), and xylenols (Xol) at different ToS.

Figure 4 compares the distribution of MA, Cr, and Xol isomers at different stages of catalyst deactivation. Their distribution changes slightly as a function of coke deposit and is noticeably different from the thermodynamic equilibrium. [39,40] For methylanisoles, while the meta position should be favoured, the main isomer is the *p*-MA. The methoxy function acts as an ortho/para directing group on the aromatic cycle (due to its +M mesomeric effect). [41] Among the 6 possible xylenol isomers, 2,4-xylenol with one methyl in ortho position, and another on in para of the hydroxyl group, is the most abundant. The additional shape selectivity of the MFI framework promotes the formation of para isomers. The higher the coke content, the higher the para selectivity, due to the neutralization of the non-selective outer acid sites, as already observed for xylenes[42].

The hydroxyl group has a stronger electron donation effect (+M) than the methoxy group, leading to higher selectivities for cresol's para and ortho isomers. Moreover, the impact of product shape

selectivity on methylphenols is lesser than with methylanisoles, because they are smaller and therefore diffuse more rapidly.

Xylenol has six isomers, but the resonance effect of the hydroxyl function combined with the "product shape selectivity" of the zeolite results in high 2,4-xylenol (o,p-) selectivity (> 85%), mainly on the deactivated catalyst.

The disproportionation of anisole is a Friedel-Crafts-like alkylation between two anisole molecules. The reaction begins with the formation of an oxonium ion by protonation of an anisole molecule on the BAS (step ①). This oxonium ion, with its strong attractor inductive effect, allows a π electron pair on another anisole (in the gas phase) aromatic ring to reach the carbon of the methoxy group, leading to the O-C bond cleavage (step ②). This produces phenol, as well as an arenium ion. The latter is converted to methylanisole by regeneration of the BAS (step ③). The methoxy group is an ortho/para-directing group, thus the formation of meta-methylanisole is greatly limited (para>ortho for steric hindrance reasons).

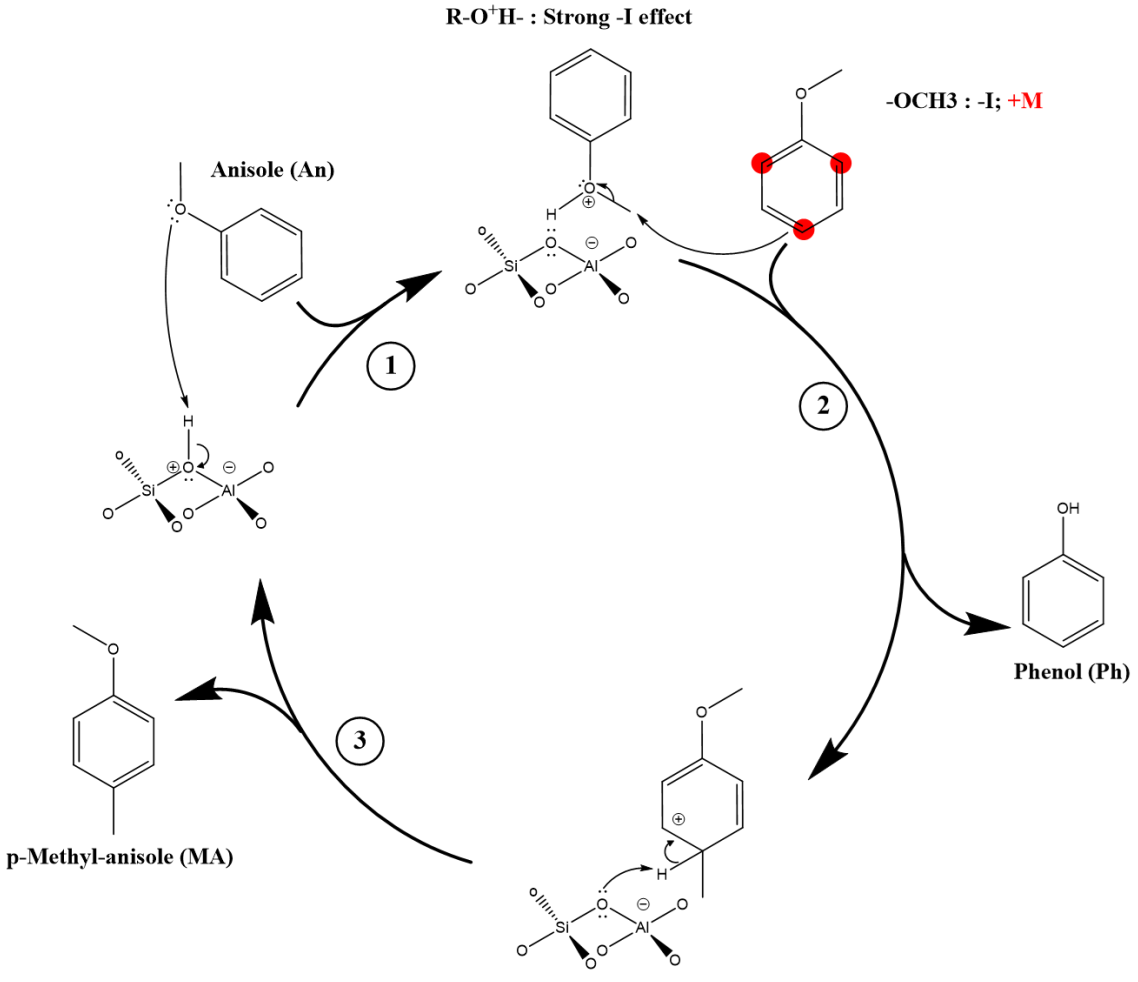

Scheme 1: Anisole disproportionation on zeolite: a Friedel-Crafts-like reaction mechanism.

Anisole disproportionation leads to the formation of *p*-methylanisole and phenol (primary products) which can comproportionate to *p*- and *o*- cresols (secondary product). The latter can also result from a transalkylation reaction between anisole and phenol. A transalkylation reaction is also possible between anisole and the secondary product, yielding mainly 2,4-xylenol (o-,p-).

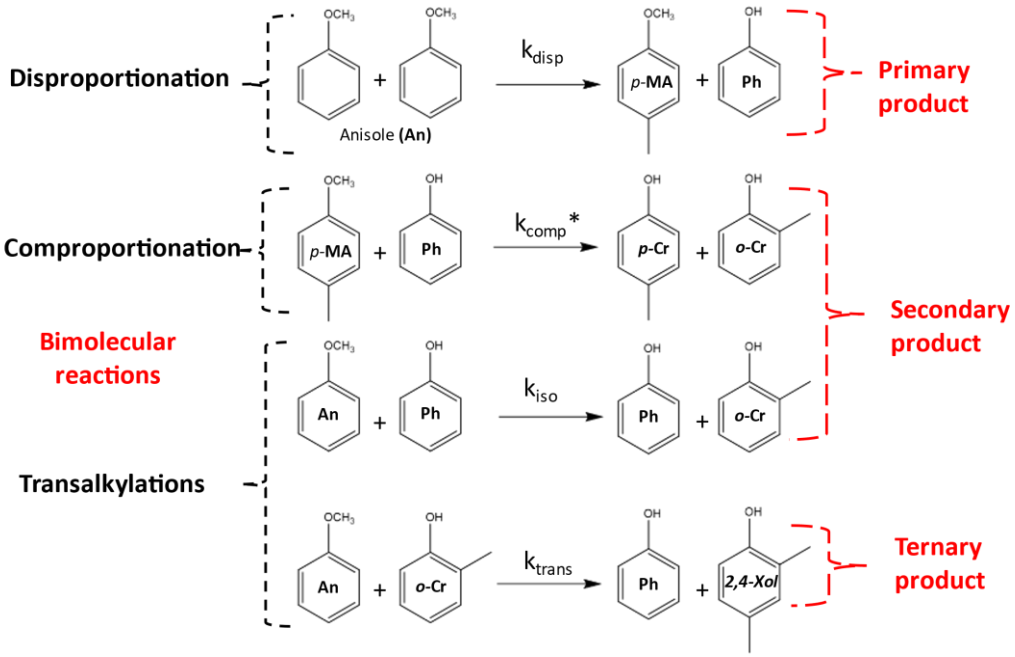

Scheme 2: Bimolecular reactions involved in anisole transformation.

Coke composition: The main issue for anisole transformation, as for CFP and in general FCC, is catalyst deactivation by coke formation in zeolite micropores and/or its deposition on external surface. Prior to coke analysis, loosely adsorbed reaction products are first removed by nitrogen stripping for 15 min.

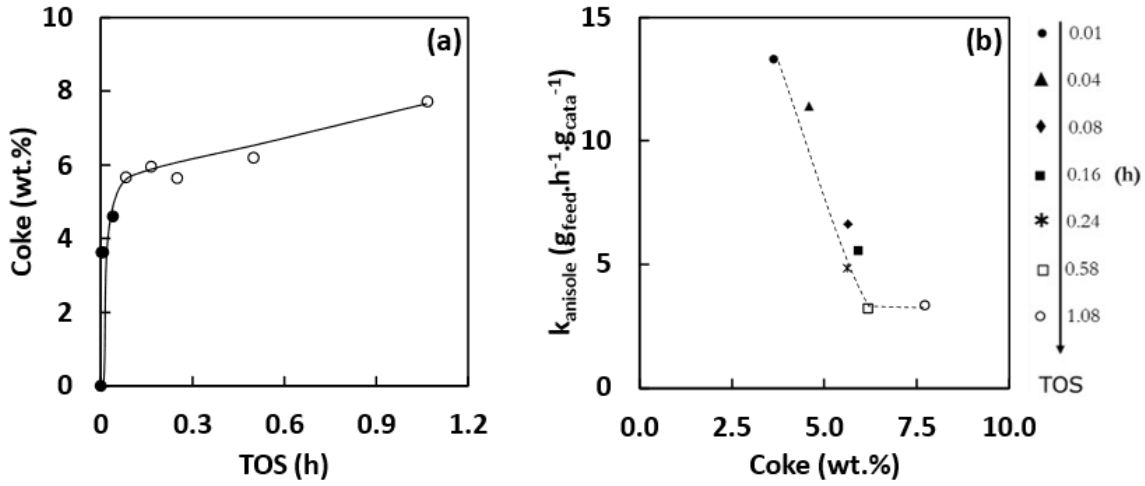

Figure 5: **(a)**: Coke content (wt.%) as a function of time-on-stream **(b)**: Kinetic rate of anisole transformation as a function of coke content.

Figure 5a shows the time evolution of coke content with a W/F of 0.13 $g_{cata}.h$. g_{feed}^{-1}. A fast coke build-up (6 wt.% within 3 minutes) is followed by a slower step. The kinetic rate constant of anisole transformation is first inversely proportional to coke content (**Figure 5b**) and then reaches a plateau at a higher amount (> 7 wt.%). The mode of deactivation is thus directly related to the amount of coke.

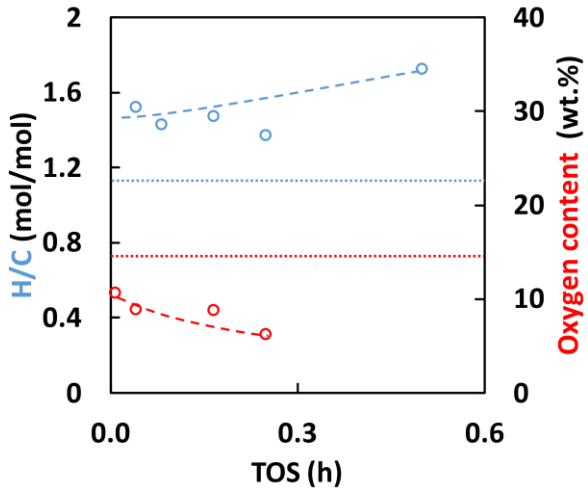

Figure 6: Time evolution of the elemental composition of the coke: hydrogen to carbon molar ratio and oxygen weight content. (Parallel dotted lines: H/C ratio and oxygen content of anisole).

Figure 6 shows the hydrogen/carbon ratio and oxygen content of coke as a function of ToS. The first coke molecules trapped in the zeolite micropores have higher H/C ratios than the reactant, it then increases with ToS, while concurrently, the oxygen content is lower than on the reactant and decreases with ToS. As olefins, xylene, benzene, have H/C molar ratios of 2, 1.25 and 1, respectively, this suggests that the coke molecules trapped in the zeolite micropores are composed of a single-ring aromatic with one hydroxyl group and/or methyl groups. These coke molecules originate from the successive transalkylation of anisole and their resulting products.

The chemical composition of coke is obtained after mineralization of the zeolite framework with concentrated hydrofluoric acid, followed by liquid-liquid extraction with dichloromethane. All coke molecules recovered are soluble in CH_2Cl_2, even at high coke content. The hydrofluoric acid used for the dissolution of the zeolite framework is a weak acid, used mainly in organic chemistry for the fluorination of organic molecules [43–45]. The reactivity of HF on oxygenated molecules is low, both for fluorination and alcohol dehydration. In addition, the extraction is performed at room temperature and for a short period of time [47], thus avoiding any side reactions.

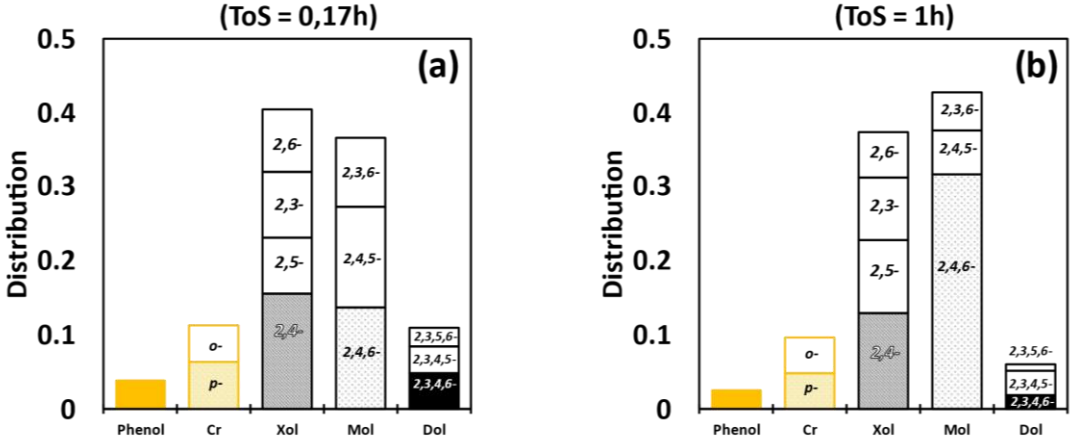

***Figure 7**:* Distribution of the coke components (isomers and families) at ToS of 0.17 h **(a)** and 1 h **(b)**.

Figure 7 compares the composition of the coke extracted after short and longer ToS. Regardless of ToS, the coke consists almost exclusively of phenolic rings substituted with 0 to 4 methyl groups. There are no ethers or polyaromatics, even after 1 h. The phenolic compounds appear to hinder the growth mechanisms of “traditional” coke. As coking is a shape-selective process [46], the size and shape of the H-ZSM-5 channel intersections determine the shape and maximum size of the coke molecules trapped in its microporosity. Irrespective of the reactant, (alkanes [47], olefins [48],

aromatics, and alcohols [49]), the coke trapped at the channels intersection is composed of methylpyrenes [50]. Coke formation progresses by successive expansions and contractions of the methylated aromatic ring with the growth of a side carbon chain (Sullivan mechanism). When the side carbon chain contains 5 carbon atoms, an auto-alkylation occurs and, after hydride transfer, produces a new aromatic ring. However, with anisole dismutation, coke consists only of phenolic compounds. The absence of polyaromatic compounds suggests that the hydroxyl group hinders the expansion/contraction mechanism, caused by a mesomeric effect. Only successive transalkylation reactions take place and lead mainly to the formation of mesitol (Mol: trimethylphenol) and to a lesser extent durenol (Dol: tetramethylphenol) (**Figure 7**). Their retention is obviously due to steric constraints.

Among the coke molecules, some reaction products such as phenol, cresols, and xylenols are found, despite N_2 stripping. However, the isomer distribution differs between desorbed and trapped molecules. While the desorbed xylenol is mainly the 2,4- isomer (**Figure 4**), the trapped molecules are composed of 4 of the six possible isomers: 2,3-, 2,4-, 2,5- and 2,6-. 2,4-xylenol remains the main isomer but in a lower proportion. The presence of reaction products among the coke molecules means that their retention is not due to steric constraints but to chemical retention. Desorption and retention of the same molecule demonstrate heterogeneity in the strength of the adsorption sites, *i.e.,* the Brønsted acid sites (BAS). Strong BAS would retain a reactant while weaker ones are active in the Friedel-Craft reaction.

Computed adsorption energies of phenolic compounds: Among the 12 distinguishable T sites in H-ZSM-5 zeolite, T11 (equivalent to T5) and T12 (equivalent to T6) were selected as the most representative T sites**.** [34,35] **Table 1** compares the adsorption energies, ΔE_{ads}, and the contribution of London dispersion interactions, $\Delta E_{disp,}$ on T11 and T12 aluminium atoms of some selected molecules. All the adsorption energies are negative, implying their exothermic nature.

Table 1: Comparison of adsorption energies and the contribution of London dispersion interaction of selected molecules on T11 and T12 atoms.

	ΔE_{ads} (kJ.mol^{-1})		ΔE_{disp} (kJ.mol^{-1})		Length	Width	σ	
Compound	T11	T12	T11	T12	(Å)		(Å²)	pK_A[a]
An	**-110.0**	**-133.7**	**-118.4**	**-106.2**	**7**	**4.3**	**30.1**	
o-MA	-108.8	-104.1	-146.1	-151.2	7	5.5	38.5	
m-MA	-137.0	-145.1	-112.4	-132.7	7.4	4.9	36.3	

p-MA	-139.1	-129.0	-131.5	-132.9	8.0	4.3	34.4	
Ph	-82.1	-100.6	-100.0	-109.4	5.7	4.3	24.5	9.95
o-Cr	-103.0	-114.6	-113.2	-118.5	5.9	4.6	27.1	10.28
m-Cr	-90.2	-116.1	-124.4	-109.0	6.2	4.9	30.4	10.09
p-Cr	-110.5	-124.9	-108.0	-113.2	6.7	4.3	28.8	10.26
2,4-Xol	-96.0	-123.7	-130.5	-169.6	6.7	5.5	36.9	10.45
2,5-Xol	-110.9	-123.0	-127.4	-120.6	6.9	5.0	34.5	10.22
2,4,6-Mol	-11.8	-11.0	-187.2	-181.6	6.7	6.7	44.9	10.88
2,3,5,6-Dol	-4.6	-7.4	-197.3	-207.8	6.9	6.7	46.2	10.88
benzene	-71.4	-28.0	-100.7	-94.6	5.0	4.3	21.5	
toluene	-74.6	-67.8	-103.5	-108.0	5.9	4.3	25.4	

[a]: values from CRC Handbook of Tables for Organic Compound identification, third edition, 1984, ISBN 0-8493-0303-6. For Mesitol: https://www.chemicalbook.com/ProductMSDSDetailCB3682841_EN.htm (consulted 09/05/2023). For Durenol: https://www.guidechem.com/encyclopedia/2-3-5-6-tetramethyl-phenol-dic370230.html (consulted 09/05/2023).

Figure 8 displays the final geometries of ether and phenolic molecules on Al12 acid site. Ethers, anisole and *m*-methyl anisole, lead to the formation of a hydrogen bond between the oxygen of the adsorbates and the hydrogen of the BAS. On phenolic compounds, regardless of the number of methyl group, a second hydrogen bond appears between the hydrogen of the hydroxyl group and an oxygen atom of zeolite. The adsorption energies of oxygenated molecules are higher than that of aromatics owing to the presence of hydrogen bond. But, despite additional hydrogen bonds, the adsorption energy stays higher (in absolute value) on ether molecules than on phenolic molecules.

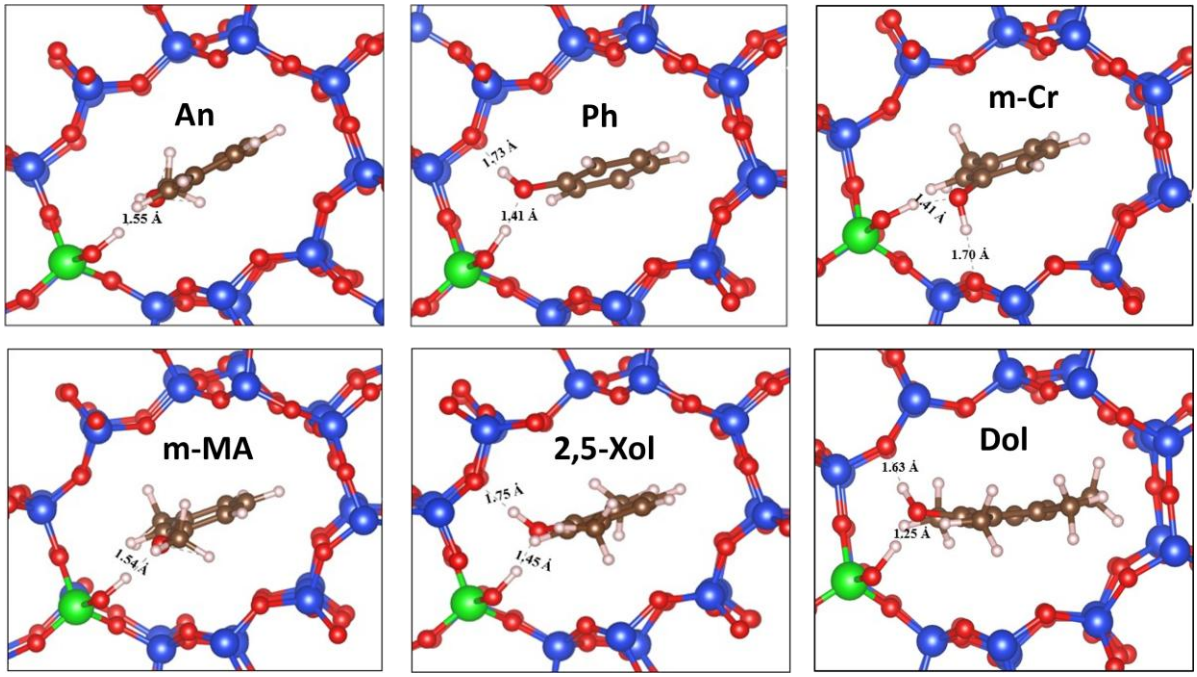

Figure 8: Final geometries of anisole, m-methylanisole and phenolic compounds adsorbed on Al12 acid site. Dashed lines represent hydrogen bonds.

On phenol, cresols and xylenols molecules, ΔE_{ads} depends on their pk_A value; the higher the basic strength (higher pK_A), the higher the adsorption energies (in absolute value) (**Figure 9a**). Moreover, ΔE_{ads} is always 15-20 $kJ.mol^{-1}$ higher on Al12 than on Al11, demonstrating the heterogeneity of the acid sites strength. For the larger molecules, mesitol and durenol, ΔE_{ads} become very small due to a higher contribution of London dispersion interactions (in absolute value). ΔE_{disp} depends on the size of the molecule, which may be described by a simple descriptor: the parameter σ (σ = L.W ≡ $Å^2$, with L the molecule "length" and W the molecule "width" -both in Å- displayed in Table 1). $\ln|\Delta E_{disp}|$ is directly proportional to σ. (**Figure 9b**).

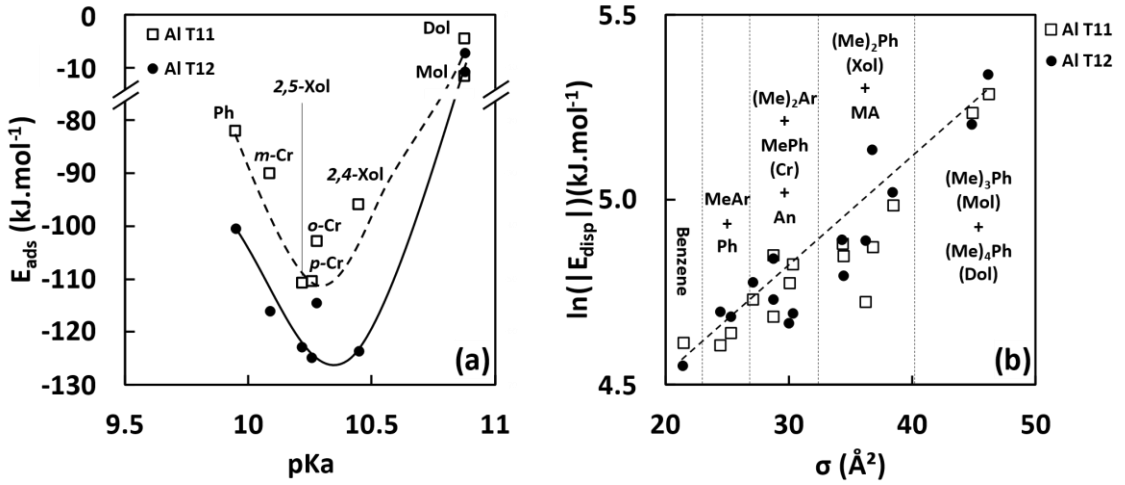

Figure 9: Evolution of **(a)** adsorption energies with pKa for phenolic molecules and **(b)** natural logarithm of dispersion energies with the σ steric parameter for each molecule, on sites T11 and T12

GC-MS and FID show no anisole or derivatives in the coke, while DFT indicates they are more easily adsorbed on BAS than phenol. Even when these "coke" molecules completely occupy any and all available sites, anisole should competitively adsorb against phenol and other weakly adsorbed compounds. This is not the case, and indicates that anisole, when adsorbed onto an acid site, is automatically transformed by transalkylation, participating to the steady-state conversion, and also the further methylation of phenolics in coke, while producing the "base" phenol. Moreover, while phenol has been shown to inhibit anisole disproportionation[51], the stronger adsorption energies of anisole, when compared to phenolics, explains the steady-state previously discussed: Anisole competitively adsorbs on BAS against these phenolics, allowing for its continued transformation.

Toxicity of the oxygenated coke molecules: The coke formed during anisole transformation is composed mostly of methylated phenols, the main products of successive transalkylations. The fundamental difference between the carbon deposition observed here and the one in FCC begs the following question: How does carbon deposition affects the textural properties, and deactivation mode of the HZSM-5 during the transformation of anisole?

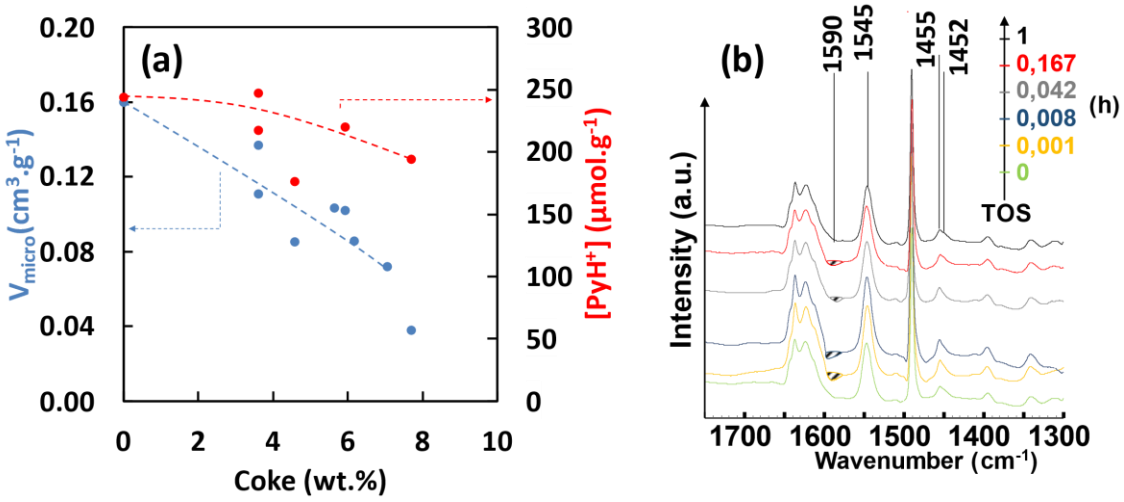

Figure 10: **(a)** Concentration of Brønsted acid sites and micropore volume as a function of coke content **(b)** IR signature of coke displacement by pyridine in MFI.

Figure 10a shows the residual concentration of BAS and micropore volume as a function of coke content. The microporosity loss is proportional to coke content, while the BAS concentration is less affected. The discrepancy could be explained in part by an overestimation of the concentration of the acidic sites actually accessible [52]. Indeed, basic pyridine could displace less basic molecules (phenolics) adsorbed on BAS; however, such competition appears limited (negative peak at 1590 cm-1, **Figure 10b**).

This does not fully explain the above discrepancy, as a loss of access to micropore volume should mean an equal loss of access to the sites contained within that volume. The computed average molecular mass of coke (114 $g.mol^{-1}$, GC-FID of the soluble coke) is a way to estimate the number of coke molecules per BAS. This mass is relatively low, when compared to those obtained in other hydrocarbon conversion processes [53,54], or even biomass conversion [16,55], >130-220 and 340 $g.mol^{-1}$ respectively. [6,56] **Figure 11a** shows that the number of coke molecules in the zeolite very rapidly reaches twice the number of accessible BAS, meaning that coke deposition leads to progressive fouling rather than acid site poisoning. [57]

The average coke density can be derived from GC-FID of soluble coke (0.930 $g.cm^{-3}$) to assess the actual volume occupied by coke in the zeolite. As shown by **Figure 11b**, it is roughly equal to the one given by N_2-physisorption, except at later TOS, and higher coke contents. It implies that coke obstructs more volume than it physically occupies. This confirms the fouling proposed by Prasomsri et al. [16], with pore plugging starting at higher coke contents.

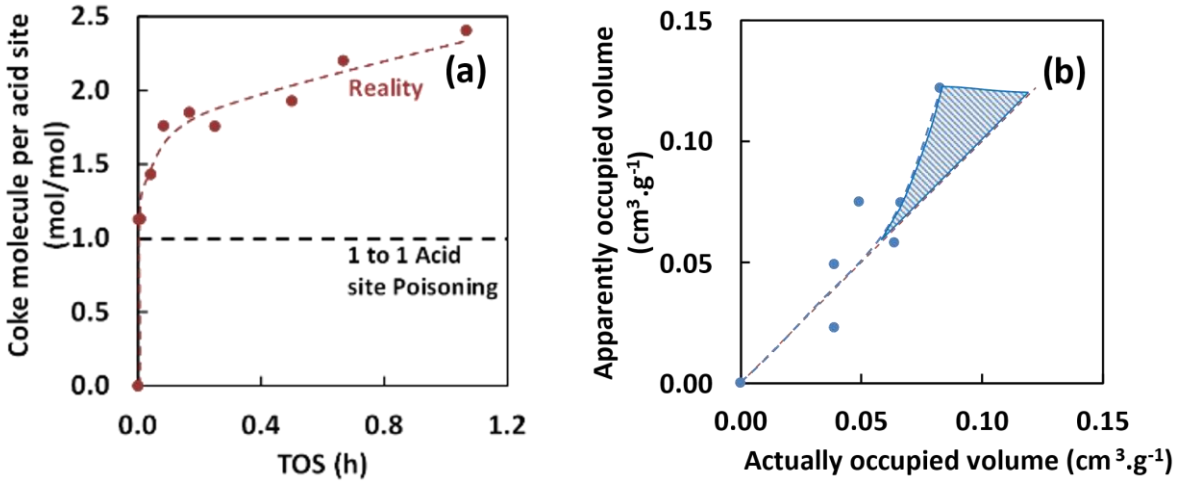

Figure 11: **(a)** Assessment of the number of "coke" molecules per available acid sites on the fresh catalyst; **(b)** Comparison between the measurable microporous volume inaccessible to N_2-Physisorption (i.e., the apparently occupied volume) and the calculated volume, actually occupied by the "coke" molecules.

Conclusion:

The transformation of anisole on HZSM-5 (Si/Al = 43) at 673 K under atmospheric pressure, a proxy for lignocellulosic biomass catalytic fast pyrolysis, is followed with particular attention to product selectivity, reaction kinetics and catalyst deactivation. An apparent first-order reaction rate is evidenced. A strong shape selectivity is evidenced, due to electronic (mesomeric and inductive) as well as steric (zeolite shape selectivity and molecule size) effects. The catalyst deactivates by a strong retention of (methyl)phenols (reaction products), rather than the more usual coking (production and deposition of polyaromatics). Phenol and its methylated products are strongly adsorbed on the catalyst, as expected from their size and pKa, leading to catalyst fouling, rather than the often observed active (acid) sites poisoning. While the CFP process is often compared to FCC, its operating conditions, mainly temperature (673 K vs 823 K for typical FCC), are considerably milder and explain the absence of polycyclic " hard coke". Such a feature is likely to facilitate catalyst regeneration.

Catalyst regeneration could be either combustion, as in FCC, or with (partially or not) oxidative plasma, or even by extracting the "coke" molecules, with an appropriate hydrogen-donor solvent. Optimization of this important step could significantly affect the overall process productivity and heat balance.

Acknowledgements

Nathan Pichot would like to thank the French Agence Nationale de la Recherche (ANR) and Région Nouvelle-Aquitaine for their financial support, through the PYCASSO and SHAPING projects. Similarly, Ludovic Pinard thanks the Région Normandie for their financial support, through the Bio/DNH project.

The authors thank the Xylofutur label for their support.

The authors acknowledge the precious work and help of Jean-Dominique Comparot (IC2MP, Poitiers) on Pyridine-FTIR and N_2-Physisorption analyses, as well as those of Morgane Vilette (IC2MP, Poitiers), for her work on elemental analysis of the "coked" catalysts.

Declaration of competing interests

The authors declare having no known competing financial or personal interests that could have influenced the work and results discussed in the present paper.

Authors contribution credit

Nathan Pichot: Experimental work, data exploitation, first draft, review, editing.

Jean Wilfried Hounfodji, Michael Badawi: DFT Calculations.

Svetlana Mintova, Valentin Valtchev: Review, editing.

Jean-Pierre Gilson: Discussion, review, editing.

Anthony Dufour: Supervision, funding, review, and editing.

Ludovic Pinard: Supervision, design of experimental work, data exploitation, funding, review, and editing

References

[1] E.J. Cho, L.T.P. Trinh, Y. Song, Y.G. Lee, H.-J. Bae, Bioconversion of biomass waste into high value chemicals, Bioresource Technology. 298 (2020) 122386. https://doi.org/10.1016/j.biortech.2019.122386.

[2] J.S.M. Samec, Holistic Approach for Converting Biomass to Fuels, Chem. 4 (2018) 1199–1200. https://doi.org/10.1016/j.chempr.2018.05.010.

[3] E.F. Iliopoulou, K.S. Triantafyllidis, A.A. Lappas, Overview of catalytic upgrading of biomass pyrolysis vapors toward the production of fuels and high-value chemicals, WIREs Energy Environ. 8 (2019). https://doi.org/10.1002/wene.322.

[4] O. Ezekoye, H. Lavandier, C. Lorbeer, W. Rehm, J. Wallach, Chemicals and capital markets: Growing sustainably, (2022). https://www.mckinsey.com/industries/chemicals/our-insights/chemicals-and-capital-markets-growing-sustainably#/ (accessed March 7, 2023).

[5] S. Alfano, F. Berruti, N. Denis, A. Santagostino, The future of second-generation biomass, (n.d.).

[6] L.Y. Jia, M. Raad, S. Hamieh, J. Toufaily, T. Hamieh, M. Bettahar, G. Mauviel, M. Tarrighi, L. Pinard, A. Dufour, Catalytic fast pyrolysis of biomass : superior selectivity of hierarchical zeolite to aromatics, Green Chem. 19 (2017) 5442–5459. https://doi.org/10.1039/C7GC02309J.

[7] T.R. Carlson, G.A. Tompsett, W.C. Conner, G.W. Huber, Aromatic Production from Catalytic Fast Pyrolysis of Biomass-Derived Feedstocks, Top Catal. 52 (2009) 241–252. https://doi.org/10.1007/s11244-008-9160-6.

[8] T.R. Carlson, Y.-T. Cheng, J. Jae, G.W. Huber, Production of green aromatics and olefins by catalytic fast pyrolysis of wood sawdust, Energy Environ. Sci. 4 (2011) 145–161. https://doi.org/10.1039/C0EE00341G.

[9] V.B.F. Custodis, S.A. Karakoulia, K.S. Triantafyllidis, J.A. van Bokhoven, Catalytic Fast Pyrolysis of Lignin over High-Surface-Area Mesoporous Aluminosilicates: Effect of Porosity and Acidity, ChemSusChem. 9 (2016) 1134–1145. https://doi.org/10.1002/cssc.201600105.

[10] D.C. Dayton, J.R. Carpenter, A. Kataria, J.E. Peters, D. Barbee, O.D. Mante, R. Gupta, Design and operation of a pilot-scale catalytic biomass pyrolysis unit, Green Chem. 17 (2015) 4680–4689. https://doi.org/10.1039/C5GC01023C.

[11] J. Jae, G.A. Tompsett, A.J. Foster, K.D. Hammond, S.M. Auerbach, R.F. Lobo, G.W. Huber, Investigation into the shape selectivity of zeolite catalysts for biomass conversion, Journal of Catalysis. 279 (2011) 257–268. https://doi.org/10.1016/j.jcat.2011.01.019.

[12] T.R. Carlson, T.P. Vispute, G.W. Huber, Green Gasoline by Catalytic Fast Pyrolysis of Solid Biomass Derived Compounds, ChemSusChem. 1 (2008) 397–400. https://doi.org/10.1002/cssc.200800018.

[13] J.M. Silva, M.F. Ribeiro, I. Graça, A. Fernandes, Bio-oils/FCC co-processing: Insights into the adsorption of guaiacol on Y zeolites with distinct acidity and textural properties, Microporous

and Mesoporous Materials. 323 (2021) 111170. https://doi.org/10.1016/j.micromeso.2021.111170.

[14] I. Graça, J.M. Lopes, H.S. Cerqueira, M.F. Ribeiro, Bio-oils Upgrading for Second Generation Biofuels, Ind. Eng. Chem. Res. 52 (2013) 275–287. https://doi.org/10.1021/ie301714x.

[15] A. Aho, N. Kumar, K. Eränen, T. Salmi, M. Hupa, D.Y. Murzin, Catalytic Pyrolysis of Biomass in a Fluidized Bed Reactor, Process Safety and Environmental Protection. 85 (2007) 473–480. https://doi.org/10.1205/psep07012.

[16] T. Prasomsri, A.T. To, S. Crossley, W.E. Alvarez, D.E. Resasco, Catalytic conversion of anisole over HY and HZSM-5 zeolites in the presence of different hydrocarbon mixtures, Applied Catalysis B: Environmental. (2011) S0926337311002347. https://doi.org/10.1016/j.apcatb.2011.05.026.

[17] I.A. Vasalos, A.A. Lappas, E.P. Kopalidou, K.G. Kalogiannis, Biomass catalytic pyrolysis: process design and economic analysis, WIREs Energy Environ. 5 (2016) 370–383. https://doi.org/10.1002/wene.192.

[18] G. Yildiz, F. Ronsse, R. van Duren, W. Prins, Challenges in the design and operation of processes for catalytic fast pyrolysis of woody biomass, Renewable and Sustainable Energy Reviews. 57 (2016) 1596–1610. https://doi.org/10.1016/j.rser.2015.12.202.

[19] F.L. Mendes, V.L. Ximenes, M.B.B. de Almeida, D.A. Azevedo, N.S. Tessarolo, A. de Rezende Pinho, Catalytic pyrolysis of sugarcane bagasse and pinewood in a pilot scale unit, Journal of Analytical and Applied Pyrolysis. 122 (2016) 395–404. https://doi.org/10.1016/j.jaap.2016.08.001.

[20] I. Graça, A. Fernandes, J.M. Lopes, M.F. Ribeiro, S. Laforge, P. Magnoux, F. Ramôa Ribeiro, Bio-oils and FCC feedstocks co-processing: Impact of phenolic molecules on FCC hydrocarbons transformation over MFI, Fuel. 90 (2011) 467–476. https://doi.org/10.1016/j.fuel.2010.09.028.

[21] J.D. Adjaye, N.N. Bakhshi, Production of hydrocarbons by catalytic upgrading of a fast pyrolysis bio-oil. Part I: Conversion over various catalysts, (1995) 23.

[22] E.J. Soltes, T.A. Milne, eds., Pyrolysis Oils from Biomass: Producing, Analyzing, and Upgrading, American Chemical Society, Washington, DC, 1988. https://doi.org/10.1021/bk-1988-0376.

[23] E.F. Iliopoulou, S.D. Stefanidis, K.G. Kalogiannis, A. Delimitis, A.A. Lappas, K.S. Triantafyllidis, Catalytic upgrading of biomass pyrolysis vapors using transition metal-modified ZSM-5 zeolite, Applied Catalysis B: Environmental. 127 (2012) 281–290. https://doi.org/10.1016/j.apcatb.2012.08.030.

[24] T.C. Hoff, D.W. Gardner, R. Thilakaratne, K. Wang, T.W. Hansen, R.C. Brown, J.-P. Tessonnier, Tailoring ZSM-5 Zeolites for the Fast Pyrolysis of Biomass to Aromatic Hydrocarbons, ChemSusChem. 9 (2016) 1473–1482. https://doi.org/10.1002/cssc.201600186.

[25] M. Guisnet, P. Magnoux, D. Martin, Roles of acidity and pore structure in the deactivation of zeolites by carbonaceous deposits, in: C.H. Bartholomew, G.A. Fuentes (Eds.), Studies in Surface Science and Catalysis, Elsevier, 1997: pp. 1–19. https://doi.org/10.1016/S0167-2991(97)80138-3.

[26] L. Jia, F. Buendia-Kandia, S. Dumarcay, H. Poirot, G. Mauviel, P. Gérardin, A. Dufour, Fast Pyrolysis of Heartwood, Sapwood, and Bark: A Complementary Application of Online Photoionization Mass Spectrometry and Conventional Pyrolysis Gas Chromatography/Mass Spectrometry, Energy Fuels. 31 (2017) 4078–4089. https://doi.org/10.1021/acs.energyfuels.7b00110.

[27] Y. Le Brech, L. Jia, S. Cissé, G. Mauviel, N. Brosse, A. Dufour, Mechanisms of biomass pyrolysis studied by combining a fixed bed reactor with advanced gas analysis, Journal of Analytical and Applied Pyrolysis. 117 (2016) 334–346. https://doi.org/10.1016/j.jaap.2015.10.013.

[28] J. Ward, The nature of active sites on zeolites IX. Sodium hydrogen zeolite, Journal of Catalysis. 13 (1969) 364–372. https://doi.org/10.1016/0021-9517(69)90445-X.

[29] C. Miranda, J. Urresta, H. Cruchade, A. Tran, M. Benghalem, A. Astafan, P. Gaudin, T.J. Daou, A. Ramírez, Y. Pouilloux, A. Sachse, L. Pinard, Exploring the impact of zeolite porous voids in liquid phase reactions: The case of glycerol etherification by tert-butyl alcohol, Journal of Catalysis. 365 (2018) 249–260. https://doi.org/10.1016/j.jcat.2018.07.009.

[30] P. Magnoux, P. Roger, C. Canaff, V. Fouche, N.S. Gnep, M. Guisnet, New Technique for the Characterization of Carbonaceous Compounds Responsible for Zeolite Deactivation, (n.d.) 14.

[31] G. Kresse, J. Hafner, *Ab initio* molecular dynamics for liquid metals, Phys. Rev. B. 47 (1993) 558–561. https://doi.org/10.1103/PhysRevB.47.558.

[32] Perdew, J.P., Burke, K., and Ernzerhof, M., Generalized gradient approximation made simple., Physical Review Letters,. 77 (1996) 3865-3868.

[33] G. Kresse, D. Joubert, From ultrasoft pseudopotentials to the projector augmented-wave method, Physical Review B. 59 (1999) 1758–1775. https://doi.org/10.1103/PhysRevB.59.1758.

[34] S. Grimme, Semiempirical GGA-type density functional constructed with a long-range dispersion correction, Journal of Computational Chemistry. 27 (2006) 1787–1799. https://doi.org/10.1002/jcc.20495.

[35] S. Grimme, Accurate description of van der Waals complexes by density functional theory including empirical corrections, Journal of Computational Chemistry. 25 (2004) 1463–1473. https://doi.org/10.1002/jcc.20078.

[36] F.R. Ribeiro, M. Guisnet, Les zéolithes, un nanomonde au service de la catalyse, EDP Sciences, 2012.

[37] J.S. Magee, M.M. Mitchell, Fluid Catalytic Cracking: Science and Technology, Elsevier, 1993.

[38] M. Marczewski, J.-P. Bodibo, G. Perot, M. Guisnet, ALKYLATION OF AROMATICS PART I. REACTION NETWORK OF THE ALKYLATION OF PHENOL BY METHANOL ON USHY ZEOLITE, (n.d.) 8.

[39] M. Marczewski, G. Perot, M. Guisnet, Alkylation of Aromatics II. Alkylation of Phenol with Methanol on Various Zeolites, in: Studies in Surface Science and Catalysis, Elsevier, 1988: pp. 273–282. https://doi.org/10.1016/S0167-2991(09)60824-7.

[40] X. Zhu, R.G. Mallinson, D.E. Resasco, Role of transalkylation reactions in the conversion of anisole over HZSM-5, Applied Catalysis A: General. 379 (2010) 172–181. https://doi.org/10.1016/j.apcata.2010.03.018.

[41] T.W.G. Solomons, C.B. Fryhle, S.A. Snyder, Organic chemistry, 11e ed., Wiley, Hoboken, NJ, 2014.

[42] N.Y. Chen, Personal Perspective of the Development of Para Selective ZSM-5 Catalysts, Ind. Eng. Chem. Res. 40 (2001) 4157–4161. https://doi.org/10.1021/ie000870p.

[43] A.K. Kuriakose, J.L. Margrave, Kinetics of the Reactions of Elemental Fluorine. IV. Fluorination of Graphite, J. Phys. Chem. 69 (1965) 2772–2775. https://doi.org/10.1021/j100892a049.

[44] Y. Liu, L. Jiang, H. Wang, H. Wang, W. Jiao, G. Chen, P. Zhang, D. Hui, X. Jian, A brief review for fluorinated carbon: synthesis, properties and applications, Nanotechnology Reviews. 8 (2019) 573–586. https://doi.org/10.1515/ntrev-2019-0051.

[45] M. Dubois, N. Batisse, K. Guérin, P. Thomas, Fluorine: Characteristics, Chemistry and Applications Controlled fluorination using atomic fluorine, (n.d.).

[46] M. Guisnet, J.-P. Gilson, Zeolites for Cleaner Technologies, Imperial College Press, 2005. https://doi.org/10.13140/2.1.3317.8401.

[47] M. Raad, A. Astafan, S. Hamieh, J. Toufaily, T. Hamieh, J.D. Comparot, C. Canaff, T.J. Daou, J. Patarin, L. Pinard, Catalytic properties of Ga-containing MFI-type zeolite in cyclohexane dehydrogenation and propane aromatization, Journal of Catalysis. 365 (2018) 376–390. https://doi.org/10.1016/j.jcat.2018.06.029.

[48] A. Bonnin, Y. Pouilloux, V. Coupard, D. Uzio, L. Pinard, Deactivation mechanism and regeneration study of Zn/HZSM-5 catalyst in ethylene transformation, Applied Catalysis A: General. 611 (2021) 117976. https://doi.org/10.1016/j.apcata.2020.117976.

[49] F. Ferreira Madeira, K. Ben Tayeb, L. Pinard, H. Vezin, S. Maury, N. Cadran, Ethanol transformation into hydrocarbons on ZSM-5 zeolites: Influence of Si/Al ratio on catalytic performances and deactivation rate. Study of the radical species role, Applied Catalysis A: General. 443–444 (2012) 171–180. https://doi.org/10.1016/j.apcata.2012.07.037.

[50] M. Guisnet, F.R. Ribeiro, eds., Deactivation and regeneration of zeolite catalysts, Imperial College Press ; Distributed by World Scientific, London : Singapore, 2011.

[51] I. Graça, J.-D. Comparot, S. Laforge, P. Magnoux, J.M. Lopes, M.F. Ribeiro, F.R. Ribeiro, Effect of phenol addition on the performances of H–Y zeolite during methylcyclohexane transformation, Applied Catalysis A: General. 353 (2009) 123–129. https://doi.org/10.1016/j.apcata.2008.10.032.

[52] I. Graça, J.-D. Comparot, S. Laforge, P. Magnoux, J.M. Lopes, M.F. Ribeiro, F. Ramôa Ribeiro, Influence of Phenol Addition on the H-ZSM-5 Zeolite Catalytic Properties during Methylcyclohexane Transformation, Energy Fuels. 23 (2009) 4224–4230. https://doi.org/10.1021/ef9003472.

[53] K. Qian, D.C. Tomczak, E.F. Rakiewicz, R.H. Harding, G. Yaluris, W.-C. Cheng, X. Zhao, A.W. Peters, Coke Formation in the Fluid Catalytic Cracking Process by Combined Analytical Techniques, (n.d.).

[54] N. Chaouati, A. Soualah, M. Chater, M. Tarighi, L. Pinard, Mechanisms of coke growth on mordenite zeolite, Journal of Catalysis. 344 (2016) 354–364. https://doi.org/10.1016/j.jcat.2016.10.011.

[55] S. Du, D.P. Gamliel, M.V. Giotto, J.A. Valla, G.M. Bollas, Coke formation of model compounds relevant to pyrolysis bio-oil over ZSM-5, Applied Catalysis A: General. 513 (2016) 67–81. https://doi.org/10.1016/j.apcata.2015.12.022.

[56] A. Beuque, M. Barreau, E. Berrier, J.-F. Paul, N. Batalha, A. Sachse, L. Pinard, Transformation of Dilute Ethylene at High Temperature on Micro- and Nano-Sized H-ZSM-5 Zeolites, Catalysts. 11 (2021) 282. https://doi.org/10.3390/catal11020282.

[57] J.W. Beeckman, G.F. Froment, Catalyst Deactivation by Active Site Coverage and Pore Blockage, Ind. Eng. Chem. Fund. 18 (1979) 245–256. https://doi.org/10.1021/i160071a009.